# Mechanisms of Tidal Oscillatory Salt Transport in a Partially Stratified Estuary

TAO WANG

*Key Laboratory of Physical Oceanography, Ministry of Education China, Ocean University of China, Qingdao, China, and Woods Hole Oceanographic Institution, Woods Hole, Massachusetts*

W. ROCKWELL GEYER

*Woods Hole Oceanographic Institution, Woods Hole, Massachusetts*

PATRICIA ENGEL

*Eastern Research Group, Arlington, Virginia*

WENSHENG JIANG AND SHIZUO FENG

*Key Laboratory of Physical Oceanography, Ministry of Education China, Ocean University of China, Qingdao, China*

(Manuscript received 10 February 2015, in final form 9 July 2015)

ABSTRACT

Tidal oscillatory salt transport, induced by the correlation between tidal variations in salinity and velocity, is an important term for the subtidal salt balance under the commonly used Eulerian method of salt transport decomposition. In this paper, its mechanisms in a partially stratified estuary are investigated with a numerical model of the Hudson estuary. During neap tides, when the estuary is strongly stratified, the tidal oscillatory salt transport is mainly due to the hydraulic response of the halocline to the longitudinal variation of topography. This mechanism does not involve vertical mixing, so it should not be regarded as oscillatory shear dispersion, but instead it should be regarded as advective transport of salt, which results from the vertical distortion of exchange flow obtained in the Eulerian decomposition by vertical fluctuations of the halocline. During spring tides, the estuary is weakly stratified, and vertical mixing plays a significant role in the tidal variation of salinity. In the spring tide regime, the tidal oscillatory salt transport is mainly due to oscillatory shear dispersion. In addition, the transient lateral circulation near large channel curvature causes the transverse tilt of the halocline. This mechanism has little effect on the cross-sectionally integrated tidal oscillatory salt transport, but it results in an apparent left–right cross-channel asymmetry of tidal oscillatory salt transport. With the isohaline framework, tidal oscillatory salt transport can be regarded as a part of the net estuarine salt transport, and the Lagrangian advective mechanism and dispersive mechanism can be distinguished.

## 1. Introduction

Under the commonly used Eulerian method of subtidal salt transport decomposition for estuaries, the downstream salt transport due to river outflow must be balanced on average by upstream salt transport due to the combination of estuarine exchange flow and tidal dispersive mechanisms (Pritchard 1954; MacCready 2004, 2007; MacCready and Geyer 2010). The upstream salt transport can be divided into two parts: the subtidal salt transport due to correlation between spatial variations in tidally averaged mean velocity and salinity, and the subtidal salt transport due to correlation between tidal variations in velocity and salinity (Fischer 1976; Bowen and Geyer 2003). Spatial correlation of tidally averaged velocity and salinity is usually regarded as the estuarine salt transport because it is typically driven by the estuarine exchange flow, that is, the exchange flow obtained by the Eulerian mean method (Lerczak et al. 2006; Engel 2009).

The other major contributor to upstream salt transport is related to the correlation between tidal variations

*Corresponding author address*: Tao Wang, Key Laboratory of Physical Oceanography, Ministry of Education China, Ocean University of China, Yushan Road 5, Qingdao 266003, China.
E-mail: haidawangtao@163.com

DOI: 10.1175/JPO-D-15-0031.1

in velocity and salinity, which we refer to in this paper as the tidal oscillatory salt transport. In some studies, the tidal oscillatory salt transport is considered to be caused by dispersive mechanisms (Hansen and Rattray 1965; MacCready and Geyer 2010). The common dispersive mechanisms include jet–sink flow (Stommel and Former 1952), tidal trapping (Schijf and Schonfeld 1953; Okubo 1973), tidal shear dispersion (Bowden 1965), and chaotic stirring (Zimmerman 1986). Jet–sink flow, as described by Stommel and Former (1952), describes the tidal asymmetries in flow structure and salinity resulting from the flow through an abrupt constriction (typically the mouth of a lagoonal estuary). Chen et al. (2012) used the jet–sink flow theory to explain the strong tidal oscillatory salt transport in the Merrimack estuary. Schijf and Schonfeld (1953) and Okubo (1973) proposed that lateral basins and irregular shorelines could act as lateral storing ''traps,'' which provided a peculiar mechanism for the longitudinal dispersion of salt. Taylor (1954) showed that the interaction between the vertical gradient of velocity and vertical mixing could lead to the horizontal dispersion of salt or other contaminants. This shear dispersion theory was applied in many estuarine studies to explain the mechanism of tidal oscillatory salt transport (Bowden 1965; Fischer 1976; Uncles et al. 1985; McCarthy 1993; Díez-Minguito et al. 2013). Tidal shear dispersion is important when the time scale of vertical or transverse mixing is comparable to the tidal time scale (Fischer et al. 1979; Geyer et al. 2008). Zimmerman (1986) showed that chaotic stirring could also cause the horizontal dispersion.

However, some observations of tidal oscillatory salt transport are not necessarily consistent with a dispersive mechanism. Geyer and Nepf (1996) found the large tidal oscillatory salt transport under high discharge conditions in the Hudson estuary was caused by vertical displacements of the halocline that were correlated with horizontal currents, which should not be regarded as a dispersive transport but rather a tidally distorted part of the net estuarine salt transport. Dronkers and Van De Kreeke (1986) introduced the nonlocal salt transport and suggested that it could be equated to the difference between the local salt transport in that cross section (Eulerian salt transport) and the local salt transport in the cross section moving with the tidal velocity (Lagrangian salt transport), which can be regarded as an advective mechanism. Jay (1991) thought the physical meaning of the terms of the salt transport expansions in the traditional Eulerian framework was unclear and proposed an expansion method based on Lagrangian principles.

All the above studies showed that tidal oscillatory salt transport was induced under the Eulerian decomposition method, and its mechanisms could vary.

In this paper, we use a numerical model to examine the spatial and temporal variation of tidal oscillatory salt transport in the Hudson estuary, study its mechanisms under strongly and weakly stratified conditions, discuss its relationship with the estuarine exchange flow obtained under Eulerian decomposition method, and compare with the result of an alternative decomposition method, that is, the isohaline decomposition method, which vanishes the tidal oscillatory salt transport term in the subtidal salt balance.

The paper is organized as follows: Section 2 describes the numerical model and reviews the Eulerian decomposition method. The mechanisms of tidal oscillatory salt transport in the Hudson estuary are discussed in section 3. The vertical distortion of exchange flow obtained in the Eulerian decomposition by vertical fluctuations of the halocline and the isohaline decomposition method are discussed in section 4. Finally, section 5 presents the conclusion.

## 2. Methods

### a. Numerical model

Warner et al. (2005) used the Regional Ocean Modeling System (ROMS) to develop a numerical model of the Hudson River estuary. The model in this paper is a higher-resolution version of the Warner et al. (2005) model, using idealized forcing conditions so that the tidal and residual components can be clearly separated. The model grid covers the 120-km-long river from the Battery to Poughkeepsie (Fig. 1a). The lateral resolution is 15–140 m, and the along-estuary resolution is 50–400 m. In the lower Hudson estuary, the grid spacing is approximately 200 m along the estuary and 50 m in the cross-channel direction. There are 16 terrain-following sigma layers in the vertical direction. At the northern boundary, salinity is set to zero and river discharge is set to $300\,m^3\,s^{-1}$, which is typical of low discharge conditions. At the southern boundary, water surface is forced by $M_2$ and $S_2$ tidal constituents. Because of the influence of physical processes outside of the model domain on the southern boundary and the lack of the direct measurements of salinity, the salinity and horizontal salinity gradient at the southern boundary condition are obtained by a hyperbolic tangent function fit to the along-estuary salinity distribution, following Warner et al. (2005). Surface wind stresses and low-frequency sea level fluctuations are neglected.

### b. Eulerian decomposition method

Eulerian residual velocity, the tidally averaged velocity at a fixed spatial point, is usually used to represent the residual mass transport in estuarine and

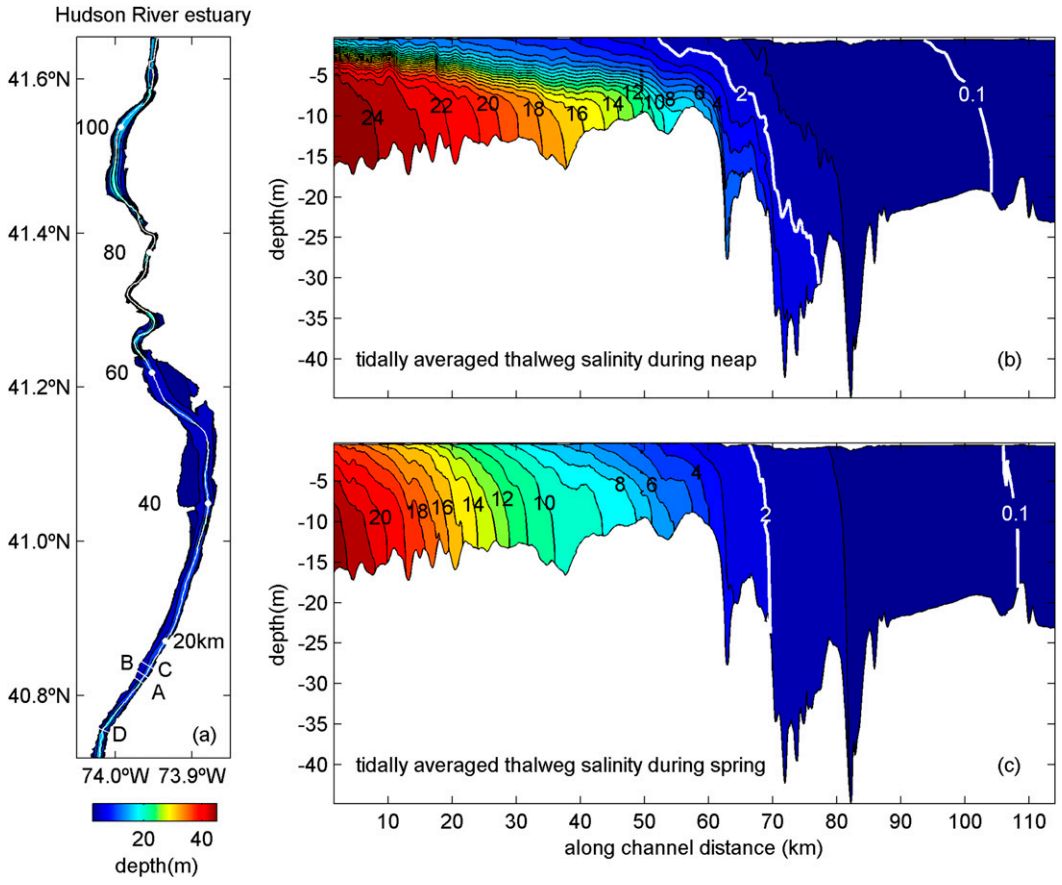


FIG. 1. (a) Model domain, the white line denotes the thalweg. The letters A, B, C, and D indicate the positions of the four cross sections chosen in section 3. Longitudinal variations of tidally averaged thalweg salinity structure during (b) neap and (c) spring tide. Horizontal axis denotes distance from model's southern boundary (the Battery). White contours indicate the 2- and 0.1-psu isohalines.

coastal studies because of the simplicity of calculation. The shortcomings of the Eulerian mean method is that the vertical variation in isohalines due to the barotropic tidal variation leads to an apparent tidal correlation salt transport term that is only the result of the barotropic distortion of the isohalines in the fixed reference frame. To make a more appropriate representation of the residual mass transport, Robinson (1983) introduced the Eulerian residual transport velocity that included the influence of the tidal variation of depth:

$$u_M = \frac{\left\langle \int_{-h_0}^{\eta} u\, dz \right\rangle}{h_0}, \tag{1}$$

where $\langle\ \rangle$ denotes the tidal averages, $u_M$ is the Eulerian residual transport velocity, $u$ is the tidal velocity, $\eta$ is the elevation of the sea surface, $h_0$ is the tidally averaged depth, and $h = h_0 + \eta$ is the water depth.

However, the method of Robinson (1983) does not effectively account for the mass transport in which there is significant vertical variation in velocity and salinity. To effectively separate the barotropic residual from the tidal oscillatory flux, a number of authors have applied a decomposition method based on the $\sigma$ coordinate (Lerczak et al. 2006; MacCready 2011; Chen et al. 2012; Giddings et al. 2014). The method is as follows.

The cross-sectional area $A$ at a particular along-channel location is divided into a constant number of differential elements $dA$ that contract and expand with the tidal rise and fall of the free surface. The tidally averaged area properties are defined as

$$dA_0 = \langle dA \rangle, \quad A_0 = \left\langle \iint dA \right\rangle, \tag{2}$$

where $\langle\ \rangle$ denotes the tidal averages and $\iint$ indicates the cross-sectional integral. For each element, its temporal longitudinal velocity $u$ and salinity $s$ are separated into

three orthogonal components: a cross-sectionally and tidally averaged component ($u_0$, $s_0$), a cross-sectionally varying and tidally averaged component ($u_E$, $s_E$), and a cross-sectionally and tidally varying component ($u_T$, $s_T$), as shown in Eq. (3):

$$u_0 = \frac{\left\langle \iint u\, dA \right\rangle}{A_0}, \quad u_E = \frac{\langle udA \rangle}{dA_0} - u_0, \quad u_T = u - \frac{\langle udA \rangle}{dA_0},$$
$$s_0 = \frac{\left\langle \iint s\, dA \right\rangle}{A_0}, \quad s_E = \frac{\langle sdA \rangle}{dA_0} - s_0, \quad s_T = s - \frac{\langle sdA \rangle}{dA_0}. \tag{3}$$

In this paper, we use a tidal low-pass filter with a half amplitude at 33 h to obtain the tidally averaged values, which is the same as Lerczak et al. (2006). The variable $u_0$ contains Stokes drift and is related to the river flow volume flux $Q_R$ by $Q_R = -u_0 A_0$. The estuarine exchange flow is $u_E$ (MacCready 2011). The variable $\langle udA \rangle / dA_0$, that is, $u_0 + u_E$, is the Eulerian residual transport velocity expanded by expressing the total cross-sectional area and velocity into its tidally averaged and varying elements, which includes the influence of the tidally varying depth in the two-layer volume transport (Giddings et al. 2014). Using equations

$$Q_{\text{in}}^{\text{Eu}} = \iint (u_0 + u_E)|_{\text{in}}\, dA_0, \quad Q_{\text{out}}^{\text{Eu}} = \iint (u_0 + u_E)|_{\text{out}}\, dA_0 \tag{4}$$

where, for example, "in" means we only count $u_0 + u_E$ in the integral when it brings water into the estuary, the subtidal inflow volume and outflow volume of exchange flow can be obtained. The variables $u_T$ and $s_T$ denote the tidally varying components and satisfy $\langle u_T dA \rangle = 0$ and $\langle s_T dA \rangle = 0$.

In this model, the intratidal longitudinal salt transport due to turbulence and subgrid-scale diffusion is negligible, compared with tidal dispersion, which is the same as other studies (Dyer 1997; MacCready 1999). Because $\langle u_T dA \rangle = 0$ and $\langle s_T dA \rangle = 0$, the tidally averaged along-channel transport of salt across a segment $dA$ of the cross section can be decomposed as

$$\begin{aligned} \langle usdA \rangle &= \langle (u_0 + u_E + u_T)(s_0 + s_E + s_T) dA \rangle \\ &= (u_0 + u_E)(s_0 + s_E) dA_0 + \langle u_T s_T dA \rangle . \end{aligned} \tag{5}$$

Therefore, the subtidal net salt transport across the cross section can be written as

$$\begin{aligned} F &= \left\langle \iint us\, dA \right\rangle = \iint \langle us\, dA \rangle \\ &= \iint (u_0 + u_E)(s_0 + s_E)\, dA_0 + \iint \langle u_T s_T\, dA \rangle \\ &= \underbrace{-Q_R s_0}_{F_R} + \underbrace{\iint u_E s_E\, dA_0}_{F_E} + \underbrace{\iint \langle u_T s_T\, dA \rangle}_{F_T} . \end{aligned} \tag{6}$$

The variable $Q_R$ is equal to the river discharge, so the term $F_R$ is usually regarded as the downstream salt transport due to river flow. Term $F_E$ indicates the spatial correlation of tidally averaged velocity and salinity. Term $F_T$, that is, the cross-sectionally integrated tidal oscillatory salt transport, is due to correlation between tidal variations of velocity, salinity, and depth. In the Hudson estuary, the tidal elevation $\Delta\eta$ relative to the tidally mean water depth $h_0$ is small, that is, $\Delta\eta/h_0 \approx 0.1 \ll 1$ and $dA/dA_0 \approx 1$, so the tidal oscillatory salt transport is mainly due to the correlation between tidal variations of velocity and salinity.

According to this decomposition, by parameterizing $F_T$ with a horizontal dispersive coefficient $K_H$ as other estuarine studies (McCarthy 1993; MacCready 2004, 2007), the one-dimensional subtidal salt balance is governed by the equation

$$\begin{aligned} &\frac{\partial s_0}{\partial t} + \frac{1}{A_0}\frac{\partial (u_0 s_0 A_0)}{\partial x} + \frac{1}{A_0}\frac{\partial \left( \iint u_E s_E\, dA_0 \right)}{\partial x} \\ &\quad = \frac{1}{A_0}\frac{\partial}{\partial x}\left( A_0 K_H \frac{\partial s_0}{\partial x} \right). \end{aligned} \tag{7}$$

## 3. Results

### a. *Temporal and longitudinal variations of exchange flow, F, $F_R$, $F_E$, and $F_T$*

The Hudson estuary varies between being strongly stratified during neap and weakly stratified during spring tides (Figs. 1b,c). This variability strongly affects the exchange flow and the subtidal salt transport, so calculations were performed for neap and spring, respectively. According to the Eulerian decomposition method described in section 2b, longitudinal variations of exchange flow, $F$, $F_R$, $F_E$, and $F_T$ during neap and spring tides in the estuary are obtained (Fig. 2).

During neap tide, the inflow volume of the exchange flow is strong (Fig. 2a) because of the strong stratification. The strong exchange flow drives net salt transport into the estuary, making the total subtidal advective salt transport $F$ landward (Fig. 2b). The inflow of exchange flow shows large and abrupt along-estuary variations

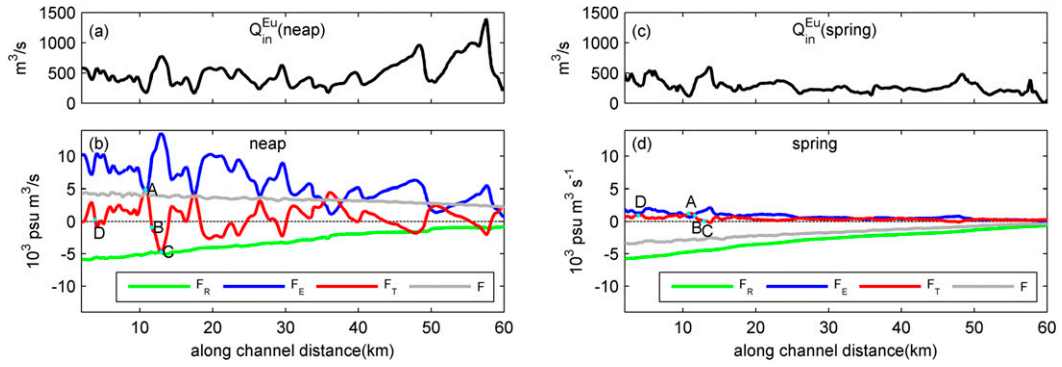


FIG. 2. Longitudinal variations of the inflow volume of (top) exchange flow, and (bottom) $F_R$, $F_E$, $F_T$, and $F$ during (left) neap tide and (right) spring tide; A, B, C, and D indicate the four cross sections chosen in section 3. The dashed line indicates zero salt flux. Positive values indicate upstream.

(Fig. 2a), which indicate there are strong divergences and convergences of the inflow volume, that is, $\partial Q_{in}^{Eu}/\partial x$. This must be balanced by cross-interface volume transport. Therefore, Eulerian exchange flow indicates that there is strong local subtidal volume transport across the interface of the two layers. In corresponding to the longitudinal variation of exchange flow, $F_E$ shows the similar variation along the channel (Fig. 2b). An important finding is that the variations of $F_E$ and $F_T$ are anticorrelated (Fig. 2b), indicating that the large variations in $F_E$ and $F_T$ compensate for each other. During neap tide, according to Eq. (7), the estimated tidal dispersion coefficient $K_H$ ranges from $-600$ to $600\,m^2\,s^{-1}$. This suggests that this decomposition is not consistent with an actual dispersion coefficient, which would be expected to be positive. The along-channel-averaged $K_H$ is about $20\,m^2\,s^{-1}$ during neap tide, which is much smaller than its longitudinal variations. The following section will focus on two questions: What is the mechanism of the large longitudinal variations of $F_T$ during neap tide and what is its relationship with the large, longitudinal variations of inflow volume of the exchange flow?

During spring tide, exchange flow is weak (Fig. 2c), so net salt transport is oceanward because of the river flow–induced residual advection (Fig. 2d). This is consistent with the results of Bowen and Geyer (2003) and Lerczak et al. (2006). The magnitudes of $F_E$ and $F_T$ are much smaller than neap tides. This is consistent with Lerczak et al. (2006). Furthermore, exchange flow, $F_E$, and $F_T$ do not show the large longitudinal variations as neap tides, and $F_T$ is almost always positive along the channel. During spring tide, the estimated along-channel-averaged tidal dispersion coefficient $K_H$ is about $30\,m^2\,s^{-1}$. The mechanism of tidal oscillatory salt transport during spring tide will be studied in section 3c.

To investigate the mechanisms of the large longitudinal variations of $F_T$ during neap tide, we choose three close sections that exhibit different amplitudes and signs of $F_T$ (Fig. 2b): strongly positive $F_T$ (section A), weak $F_T$ (section B), and strongly negative $F_T$ (section C). Their positions are also shown in Fig. 1a.

### b. *Mechanisms of $F_T$ during neap tide*

Through normalizing the tidal oscillatory salt transport across one differential element by the tidally averaged differential area $dA_0$, the cross-sectional structures of tidal oscillatory salt transport $\langle (u_T s_T dA)/dA_0 \rangle$ are obtained for the three chosen sections during neap tide (Fig. 3). To investigate the relationship between the tidal oscillatory salt transport and exchange flow, the cross-sectional structures of the Eulerian residual transport velocity $u_0 + u_E$ are also obtained (Fig. 3). Eulerian residual transport velocity is oceanward in the upper layer and landward in the lower layer for all three sections, which is consistent with the classical two-layer structure of exchange flow. At section B, the tidal oscillatory salt transport is small over all the section. At sections A and C, the strongly tidal oscillatory salt transport occurs near the interface of the inflow layer and outflow layer. This is different from the structure caused by tidal shear dispersion, which is negative near boundaries and positive away from boundaries (Larsen 1977; Ou et al. 2000; Bowen and Geyer 2003).

According to the formula used to calculate tidal oscillatory salt transport, $\langle (u_T s_T dA)/dA_0 \rangle$, the magnitude of tidal oscillatory salt transport is related to the phase differences among tidal velocity, salinity, and depth (Fischer 1972). Because $dA/dA_0 \approx 1$ in the Hudson estuary, as mentioned in section 2, the magnitude of tidal oscillatory salt transport is mainly related to the phase difference between tidal velocity and salinity. As shown in Fig. 4, when the phase difference between velocity and salinity is close to 90°, tidal oscillatory salt transport is close to 0 (Fig. 4b). When the phase difference is

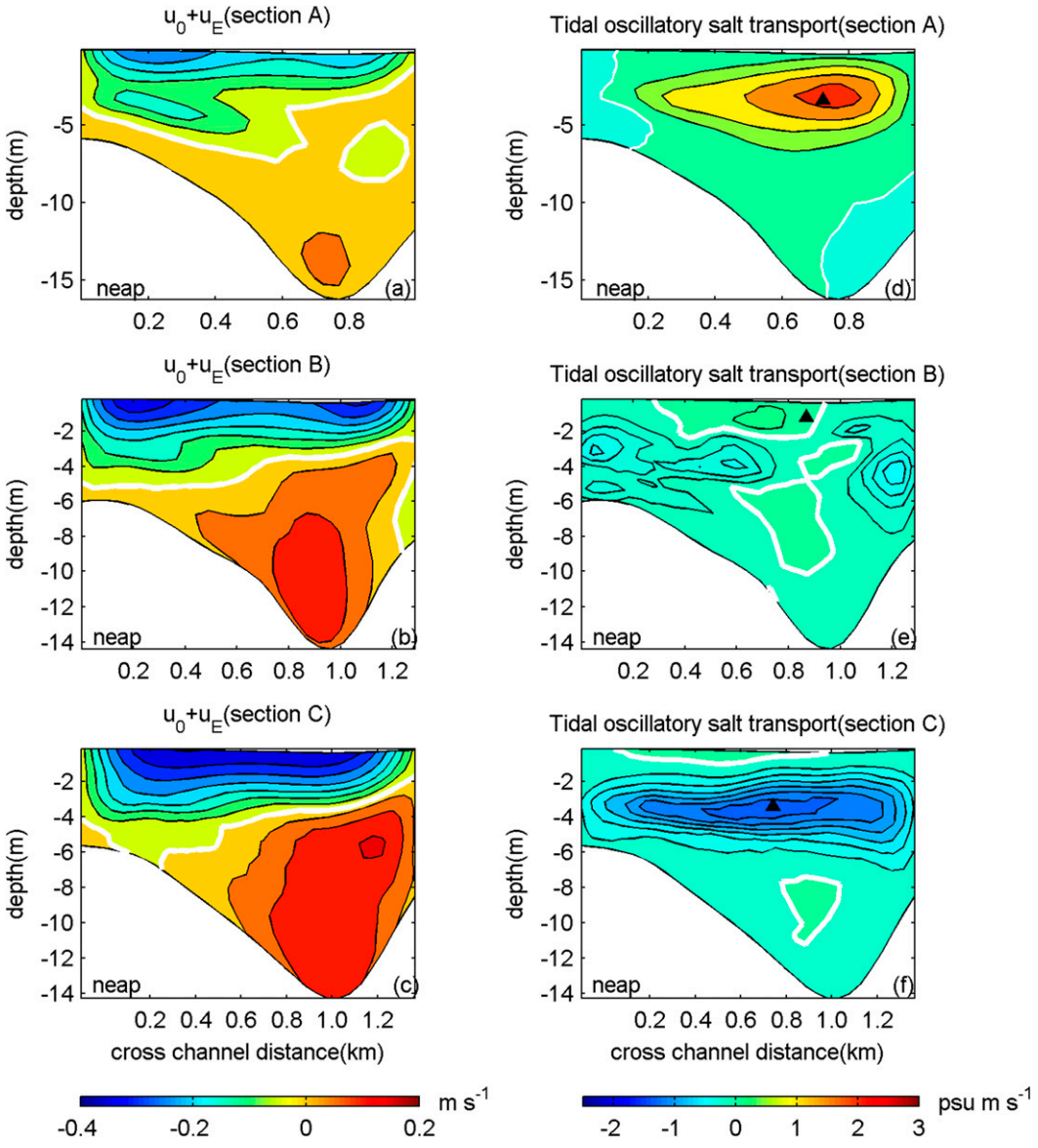


FIG. 3. Spatial structure of (a)–(c) Eulerian residual transport velocity $u_0 + u_E$ and (d)–(f) tidal oscillatory salt transport at three different kinds of sections during neap tide. Black triangles in (d)–(f) indicate the positions chosen to show the phase shift of $u_T$ and $s_T$ in Fig. 4. The unit for tidal oscillatory salt transport is psu m s$^{-1}$. Positive values indicate upstream transport. The white lines indicate zero. For $u_0 + u_E$, the white line also indicates the interface between the inflow layer and outflow layer defined by the Eulerian decomposition method.

smaller than 90°, tidal oscillatory salt transport is positive, leading to upstream salt transport (Fig. 4a). When the phase difference is larger than 90°, tidal oscillatory salt transport is negative, leading to downstream salt transport (Fig. 4c). During neap tide in the Hudson estuary, the phase difference is mainly caused by vertical fluctuations of the isohalines on tidal time scales (Fig. 5). When the phase difference between velocity and salinity is close to 90°, the heights of isohalines at maximum ebb should be nearly equal to the heights at maximum flood, as in section B. However, at section A, the isohalines with the same salinities are lower at maximum ebb than at flood, leading the phase difference between velocity and salinity to be smaller than 90°, producing positive tidal oscillatory salt transport. At section C, the isohalines with the same salinities are higher at maximum ebb than at flood, leading the phase difference between velocity and salinity to be larger than 90°, producing negative tidal oscillatory salt transport. The isohalines are closely spaced and almost parallel to each other near

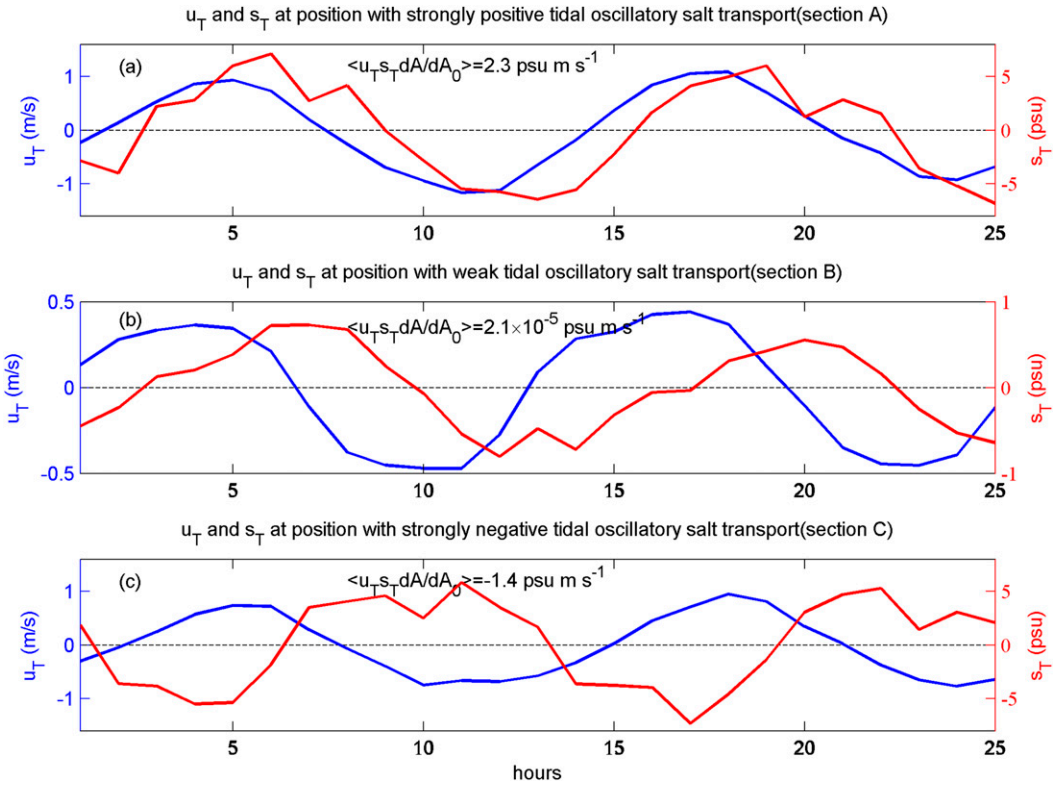


FIG. 4. (a)Tidal variations of $u_T$ (blue) and $s_T$ (red) at positions with weak tidal oscillatory salt transport, (b) strongly positive tidal oscillatory salt transport, and (c) strongly negative tidal oscillatory salt transport. The corresponding positions are shown in Figs. 3d–f.

the interface (Fig. 5), so strongly tidal oscillatory salt transport occurs near the interface.

Therefore, the strongly tidal oscillatory salt transport is related to the vertical fluctuations of the isohalines on tidal time scales. The variations of isohalines may be explained in terms of the internal hydraulic response to the estuarine topography, as mentioned by Geyer and Nepf (1996). Internal hydraulic response can cause the phase difference between vertical velocity and longitudinal velocity, which leads to the tidal asymmetry of the vertical displacements of isohalines.

To discuss the possible role of internal hydraulics causing the tidally varying elevation of isohalines during ebb and flood, we choose the region extending from 13

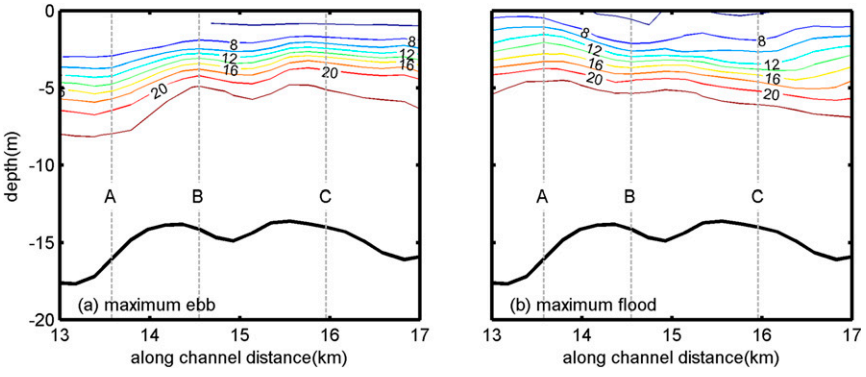


FIG. 5. Longitudinal variations of thalweg salinity structures at (a) maximum ebb and (b) maximum flood in the region 13–17 km from the Battery during neap tide. Letters A, B, and C indicate the locations of the respective sections.

to 17 km, which includes sections A, B, and C and use simplified two-layer equations to examine the influence of hydraulic effects of the estuarine geometry on the isohalines.

During neap tide, when the estuary is strongly stratified (Fig. 1b), the selected region is divided into an upper layer and lower layer. To examine the influence of hydraulic effects, we choose the 16-psu isohaline as the interface of the selected region, which is close to the interface of exchange flow. We could have selected a different isohaline, but the estimation of vertical isohaline displacement is found to be insensitive to the choice of subdivision among 12–20-psu isohalines. The volume transport between the two layers is assumed to be 0, which is a good approximation during neap tide over this 4-km reach, based on salt balance calculations. The two-dimensional schematic of the two-layer structure is shown in Fig. 6.

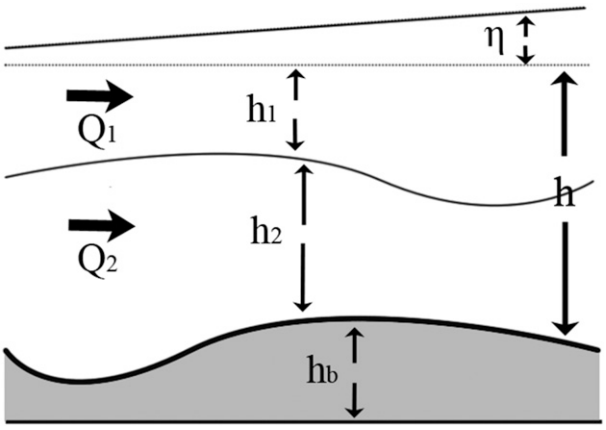


FIG. 6. Schematic of a two-layer estuary. The $z$ axis is vertically upward. The vertical position of the interface is represented with $z = -h_1$. In our calculation region, the longitudinal slope of $\eta$ is much smaller than the slope of the bottom, so $-\partial h/\partial x$ is used to represent the longitudinal variation of the bottom.

Following Geyer and Ralston (2011), the baroclinic momentum equation for the neap tide is

$$(1-G^2)\frac{\partial h_1}{\partial x} = -\frac{\partial(u_1-u_2)}{g'\partial t} + \frac{1}{g'B}\left(\frac{u_1}{h_1}+\frac{u_2}{h_2}\right)\frac{\partial Q_2}{\partial x} + F_2^2\frac{\partial h_b}{\partial x} \pm F_2^2 C_D + \frac{(u_1^2-u_2^2)}{g'B}\frac{\partial B}{\partial x} - \frac{\partial \eta}{\partial x} - \frac{C_i|(u_1-u_2)|(u_1-u_2)}{g'}\left(\frac{1}{h_1}+\frac{1}{h_2}\right), \quad (8)$$

where $x$ indicates along channel; $g' = \beta g(s_2 - s_1)$ is the reduced gravity acceleration, with the saline contraction coefficient $\beta \approx 7.7 \times 10^{-4}\,\text{psu}^{-1}$; and $C_D$ and $C_i$ denote the bottom drag coefficient and interface stress coefficient. The + case is valid during flood, and the − case is valid during ebb. The variable $B$ is the width of the channel at the water surface. The variables $h_i$, $u_i$, $s_i$, and $Q_i$ $(i = 1, 2)$ are the thicknesses, velocities, salinities, and volume fluxes of the two layers, respectively. With the output of model, they are obtained by means of weighted average: $h_i = A_i/B$, $u_i = \iint_i u\,dA/A_i$, $s_i = \iint_i s\,dA/A_i$, and $Q_i = u_i h_i B$. The variables $\eta$ and $h_b$ denote the surface and bottom elevations. Layer Froude numbers are defined by $F_1^2 = u_1^2/(g'h_1)$, $F_2^2 = u_2^2/(g'h_2)$, and $G^2 = F_1^2 + F_2^2$. The variable $G^2$ is the composite Froude number.

The local length scale is much smaller than tidal wavelength, so we obtain

$$\frac{\partial \eta}{\partial x} \ll \frac{\partial h_b}{\partial x}, \quad \frac{\partial h_b}{\partial x} = -\frac{\partial(h_1+h_2)}{\partial x} \approx -\frac{\partial h}{\partial x}. \quad (9)$$

The thickness of the upper layer $h_1$ can be obtained as the distance between interface and the free surface, and $-\partial h/\partial x$ can be used to represent the slope of the bottom, where $h$ is the water depth. The influence of surface elevation [the sixth term on the right-hand side (rhs) of Eq. (8)] is much smaller than the influence of bottom topography's variation [the third term on the rhs of Eq. (8)]. Because $C_i \ll C_D$, the interfacial stress term [the seventh term on the rhs of Eq. (8)] is much smaller than the bottom stress term [the fourth term on the rsh of Eq. (8)]; the above equation simplifies to

$$(1-G^2)\frac{\partial h_1}{\partial x} = \underbrace{-\frac{\partial(u_1-u_2)}{g'\partial t}}_{\text{TDT}} + \underbrace{\frac{1}{g'B}\left(\frac{u_1}{h_1}+\frac{u_2}{h_2}\right)\frac{\partial Q_2}{\partial x}}_{\text{VDT}} - \underbrace{F_2^2\frac{\partial h}{\partial x}}_{\text{DDT}} \pm \underbrace{F_2^2 C_D}_{\text{FDT}} + \underbrace{\frac{(u_1^2-u_2^2)}{g'B}\frac{\partial B}{\partial x}}_{\text{WDT}}, \quad (10)$$

where $\partial h_1/\partial x$ indicates the slope of interface, and $z = -h_1$ represents the vertical position of interface as shown in Fig. 6. The rhs terms in Eq. (10) are abbreviated as the time-dependent term (TDT), the volume-dependent term (VDT), the depth-dependent term (DDT), the friction-dependent term (FDT), and the width-dependent term (WDT). Term TDT is related to the time variation of vertical velocity shear. Term VDT is related to the longitudinal variation of the volume flux of the lower layer. Term DDT is associated with the bottom slope. Term FDT is due to the bottom friction, and WDT is due to the longitudinal variation of width of the estuary.

To ascertain whether the slope of the halocline is mainly due to the hydraulic response, we assume $\partial h_1/\partial x$

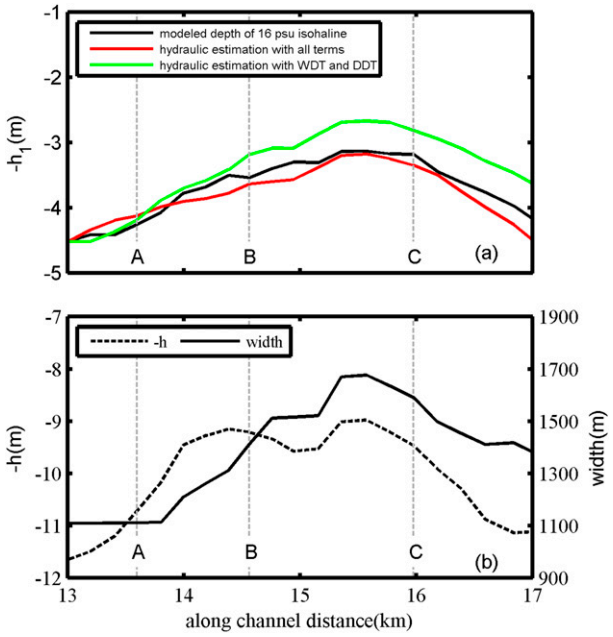


FIG. 7. (a) Hydraulic estimation of the depth of the 16-psu isohaline at maximum ebb during neap tide. Black line indicates the modeled depth of the 16-psu isohaline; red line indicates the hydraulic estimation of the depth of 16 isohaline with all rhs terms; and green line indicates the hydraulic response due to the width and depth variations. (b) Variations of width and depth. The variable $h$ indicates total water depth at maximum ebb during neap tide.

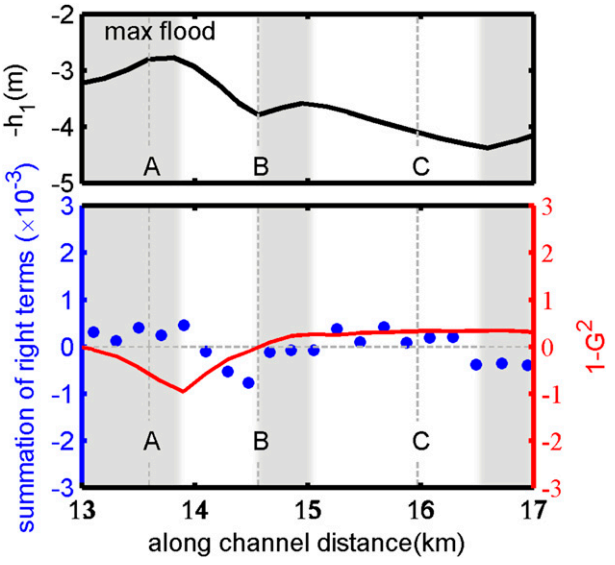


FIG. 8. Analysis of the terms in Eq. (10) affecting the slope of the 16-psu isohaline at maximum flood during neap tide within a 4-km reach of the estuary. (top) Modeled depth of 16-psu isohaline at maximum flood. (bottom) Longitudinal variation of $1 - G^2$ (red line) and summation of rhs terms in Eq. (10) (blue dots) at maximum flood. The gray regions indicate the zones where the 16-psu isohaline (interface between layers) goes up.

on the left side of Eq. (10) as the dependent variable and use other terms to calculate $\partial h_1/\partial x$ and $h_1$ and then compare with the modeled depth of the 16-psu isohaline. The comparison of the three-dimensional model representation of interface displacement with the simplified hydraulics indicates good agreement during the ebb (Fig. 7) but some discrepancy during the flood (Fig. 8).

At maximum ebb, $G^2 > 1$, that is, the flow is supercritical throughout the calculation region (Fig. 9). According to Eq. (10), we obtain the depth of interface due to hydraulic adjustment (red line in Fig. 7), which is almost equal to the modeled depth of the 16-psu isohaline (black line in Fig. 7). At maximum flood, the flow changes from supercritical condition to subcritical condition in the calculation region, and near section C, it is nearly critical, that is, $1 - G^2 \approx 0$. The time-dependent term [TDT in Eq. (10)] is more important during flood than ebb (which is not well resolved with the 1-h time step of the model output) and when calculating $\partial h_1/\partial x$, $1 - G^2$ is the denominator, the calculation error of $\partial h_1/\partial x$ becomes large as $G^2$ is nearly 1, so the estimation of $h_1$ with Eq. (10) is not well enough quantified to make a direct comparison of interface elevation as was done during the ebb. Instead of quantification for $h_1$, we calculated $1 - G^2$ and the summation of all rhs terms respectively to evaluate the relationship between hydraulic response and the modeled depth of interface (Fig. 8). When $1 - G^2$ and the summation of all rhs terms have opposite signs, $\partial h_1/\partial x < 0$, the interface goes up due to hydraulic adjustment; when $1 - G^2$ and summation of all rhs terms have the same signs, $\partial h_1/\partial x < 0$, the interface goes down. This is roughly consistent with the modeled depth of interface (Fig. 8).

This analysis thus indicates that hydraulic adjustment is a major contributor to the variation of halocline height in regions of bathymetric variability, albeit with some limitations in application to the flood tide regime. The vertical displacements of the halocline at tidal frequency are the primary cause of the tidal oscillatory salt transport. As shown in Fig. 5, when the halocline is lower at ebb than flood, positive tidal oscillatory salt transport is induced; when the halocline is higher at ebb than flood, negative tidal oscillatory salt transport is induced. Therefore, we conclude that the hydraulic response is the major contributor to the tidal oscillatory salt transport during neap tide.

Furthermore, through comparing the magnitude of rhs terms at maximum ebb, we find that in Eq. (10), the width variation term WDT is dominant because of the strong vertical velocity shear, with some significant contribution from the bottom slope term DDT and the friction term FDT. For most sections of the Hudson estuary, it narrows when deepening and expands when shoaling (Fig. 10), so WDT and DDT have the same signs for most sections during the ebb. The hydraulic estimation of interface with WDT and DDT is shown as the green line in Fig. 7a. It has

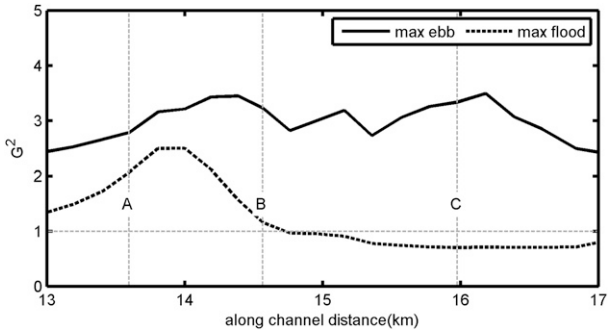


FIG. 9. Composite Froude number $G^2$ at maximum ebb and maximum flood during neap tide.

the same tendency with the modeled depth of interface. Therefore, when it is supercritical, for example, maximum ebb, the along-channel structure of isohalines approximately follows the variations of topography (Fig. 7). The negative oscillatory salt transport regions generally correspond to the regions with increasing depth and decreasing width (Fig. 10). This is not exact because the slopes of the isohalines at maximum flood are not only determined by the width and depth variations but also by time-dependence of the isohaline structure.

### c. *Mechanisms of $F_T$ during spring tide*

During spring tide, the hydraulic response becomes weaker because of the strong mixing and strong supercritical conditions, so $F_T$ no longer shows the strong bathymetric response evident during neap tides and it keeps positive along channel (Fig. 2d). As a result, the variations of $F_T$ are much smaller during the spring tides, but the spatially averaged contribution is actually significant. The mechanism for this tidal oscillatory salt transport appears to be tidal shear dispersion, as the following paragraph explains.

For the shear dispersion mechanism, the mixing perpendicular to the shear causes the phase shift between tidal velocity and salinity that vary through the cross section in such a way as to produce a net upstream salt transport (Larsen 1977; Ou et al. 2000; Bowen and Geyer 2003). The phase shift is greater than 90° in the slow-moving fluid near boundaries and less than 90° away from boundaries, inducing negative tidal oscillatory salt transport near boundaries and positive tidal oscillatory salt transport away from boundaries (Fig. 11). Because velocities away from boundaries are larger than the regions near boundaries, the absolute magnitude of positive tidal oscillatory salt transport is larger than negative tidal oscillatory salt transport, inducing positive $F_T$, that is, cross-sectional integral of tidal oscillatory salt transport (Fig. 2d). The distribution of tidal oscillatory salt transport at sections A, B, and C during spring tides shows zones of strong positive transport in the deeper, middle portions of the cross sections and negative transport in the shallower flanks,

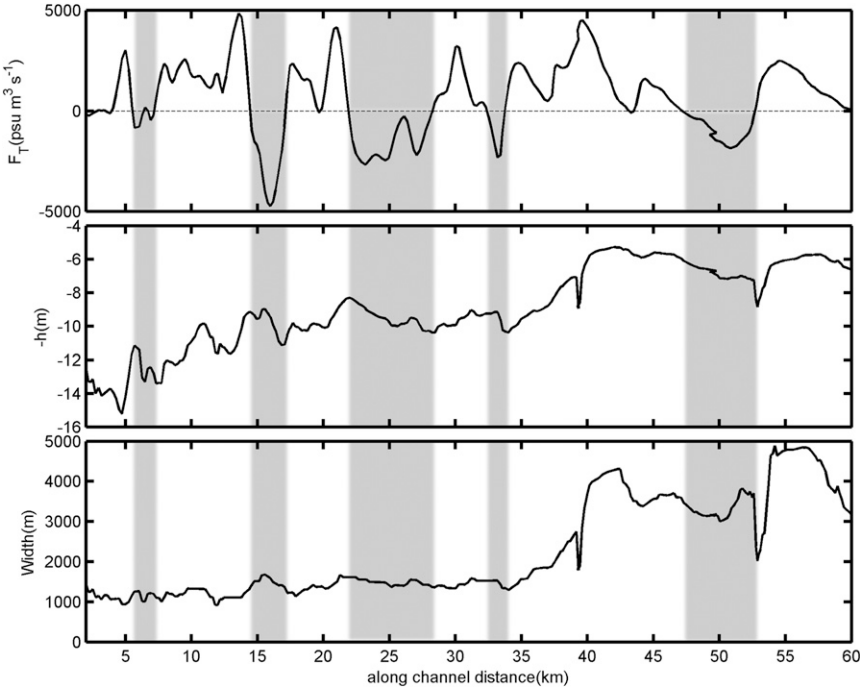


FIG. 10. Longitudinal variations of (top) $F_T$ during neap, (middle) depth, and (bottom) width. The variable $h$ indicates the water depth. Gray regions indicate negative $F_T$.

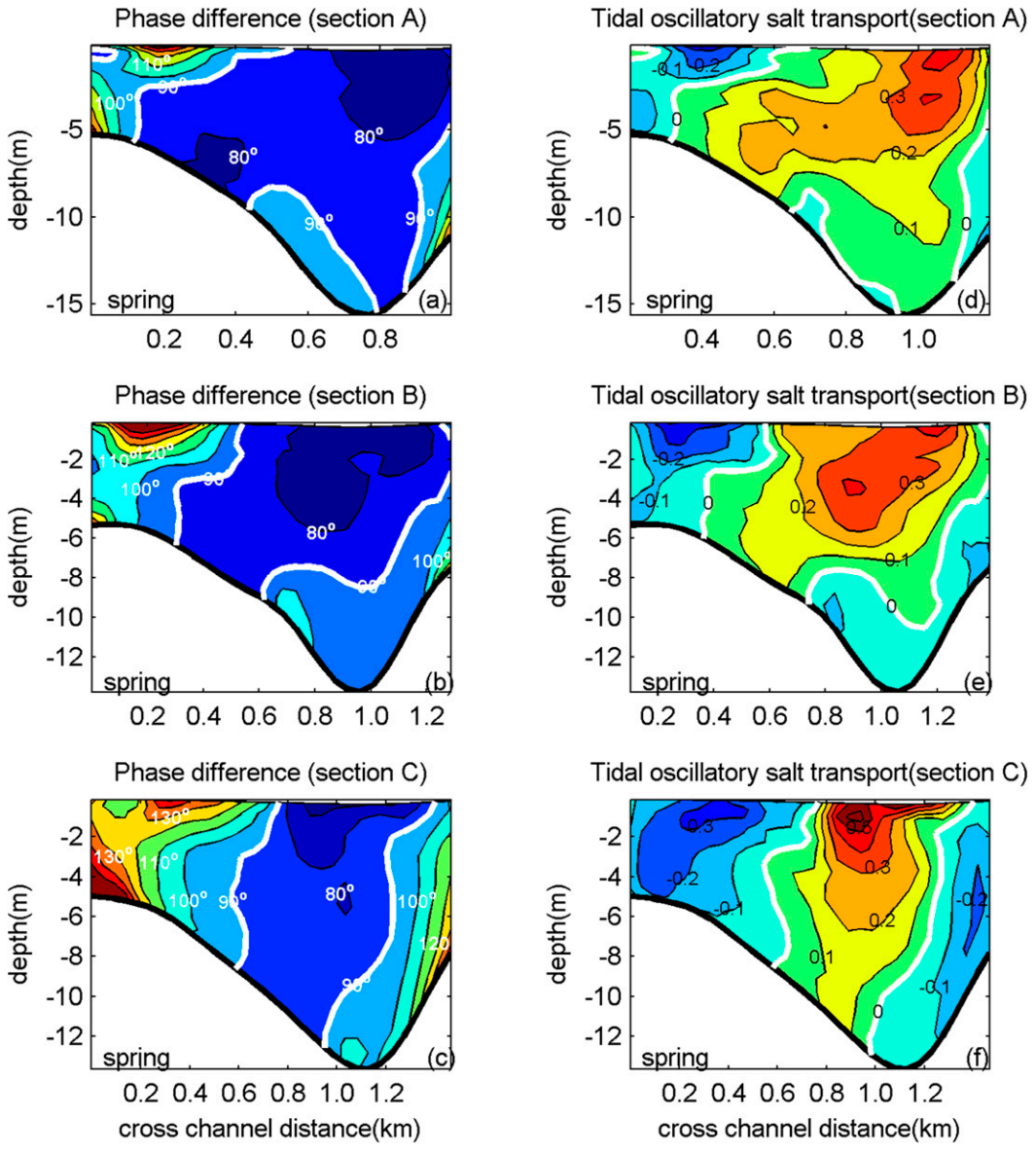


FIG. 11. (a)–(c) Phase difference of tidal velocity and salinity and (d)–(f) cross-sectional structure of tidal oscillatory salt transport (psu m $s^{-1}$) at sections A, B, and C during spring tide.

consistent with the expectation for tidal oscillatory shear dispersion.

According to Fischer et al. (1979), the dispersion coefficient $K_x$ due to vertical tidal shear dispersion is

$$K_x = \frac{u^2}{\pi^4}\frac{T^2}{T_c}\sum_{n=1}^{\infty}(2n-1)^{-2}\left\{\left[\frac{\pi}{2}(2n-1)^2\left(\frac{T}{T_c}\right)^2\right]^2+1\right\}^{-1}, \tag{11}$$

where $T$ indicates the tidal time scale, and $T_c$ is the mixing time scale. Note that $K_x$ represents the dispersion coefficient only due to the tidal shear dispersion. It is different from $K_H$ mentioned in section 2b, which is a catchall for subtidal salt transport not associated with the tidal mean exchange flow (Hansen and Rattray 1965). Here, we compare the magnitude of $K_x$ with $K_H$ to determine whether the tidal oscillatory salt transport is mainly due to tidal shear dispersion during spring tide.

The tidally and along-channel-averaged diffusivity $D$ in the halocline is estimated at about $3 \times 10^{-4}\,m^2 s^{-1}$ during spring tide in this model based on the tidally averaged diahaline salt transport. This number does not represent the vertically averaged diffusivity, but it still can yield an approximate time scale for vertical mixing, which can be determined as

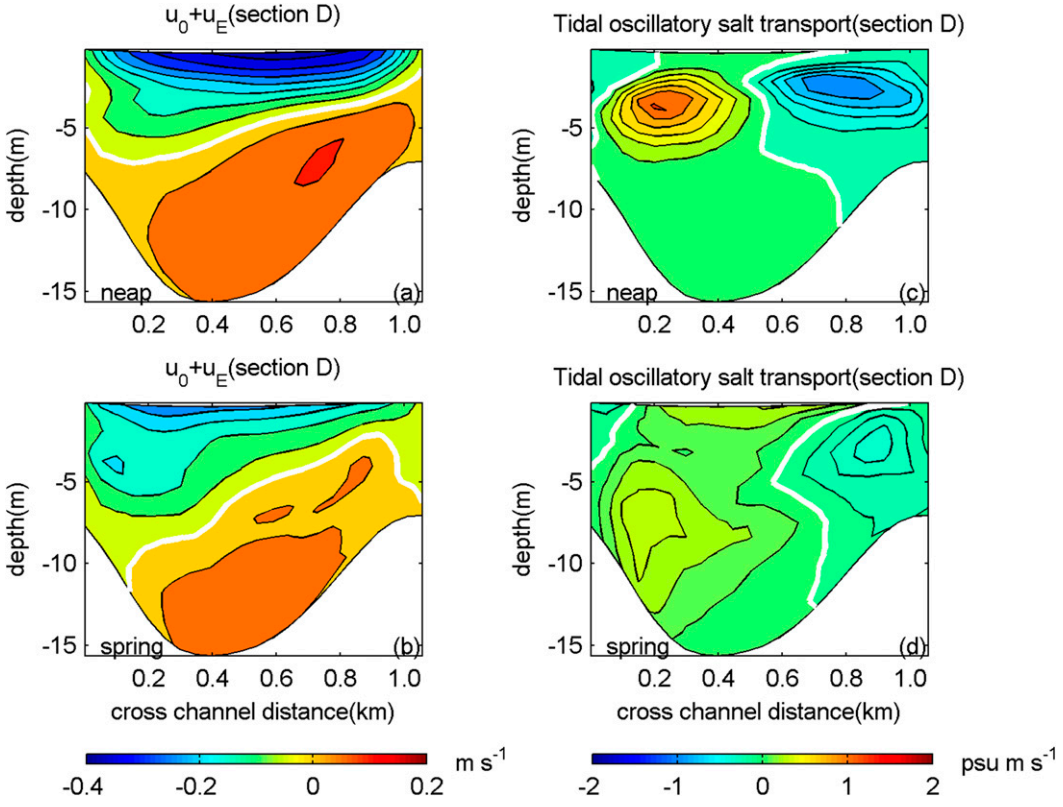


FIG. 12. Cross-sectional structures of (a),(b) Eulerian residual transport velocity and (c),(d) tidal oscillatory salt transport during neap and spring tides at section D. The strongly tidal oscillatory salt transport appears near the interface of the inflow and outflow layers.

$$T_c = h^2/10D \tag{12}$$

(Fischer et al. 1979; Geyer et al. 2008). Based on an average depth of 12 m, the mixing time scale is estimated at about 13 h, which is comparable to the tidal time scale. According to Eq. (11), the dispersion coefficient $K_x$ is estimated at about $30\,\mathrm{m^2\,s^{-1}}$. This is consistent with the along-channel-averaged $K_H \approx 30\,\mathrm{m^2\,s^{-1}}$ during spring tide. Therefore, during spring tide, when the mixing time scale is comparable to the tidal time scale, the tidal oscillatory salt transport is mainly due to the tidal shear dispersion.

### d. The contribution of transient lateral circulation

At sections near large channel curvature, the cross-sectional structure of tidal oscillatory salt transport is also influenced by the transverse tilt of isohalines. To study this mechanism, we choose section D near the large channel curvature (Fig. 1a). At section D, $F_T$ is small during both neap and spring tides (Figs. 2b,d), but tidal oscillatory salt transport has an apparent left–right cross-channel asymmetry structure near the interface, which is positive on the right side and negative on the left side (Fig. 12). As shown in Fig. 13, this is because of the transverse variation of isohalines during maximum ebb. During both neap and spring tides, at maximum ebb, there is a strongly transient lateral circulation making isohalines rise on the right side and depress on the left side. During other tidal phases, the strongly transient lateral circulation disappears and the heights of isohalines vary little in the transverse direction. The mechanism of the strongly transient lateral circulation is as follows.

As shown in Fig. 1, section D is at a location of large curvature of the estuary, so streamlines are curved around section D. During maximum ebb, the curvature induces a secondary flow that is inward to the bend at the bottom and outward at the surface because of a local imbalance between the vertically varying centrifugal acceleration and the cross-channel pressure gradient (Thorne and Hey 1979; Geyer 1993). An expression for the lateral momentum balance in a curvilinear coordinate system is

$$\frac{\partial u_n}{\partial t} + u_s\frac{\partial u_n}{\partial s} - \frac{\partial}{\partial z}\left(A_z\frac{\partial u_n}{\partial z}\right) - \frac{\tau_n}{\rho h} = -\frac{u_s^2 - \overline{u_s^2}}{R_s} - f(u_s - \overline{u_s}), \tag{13}$$

where the overbar denotes depth averaged; $A_z$ is the eddy viscosity; $\tau_n$ is the transverse bottom stress; $\rho$ is the

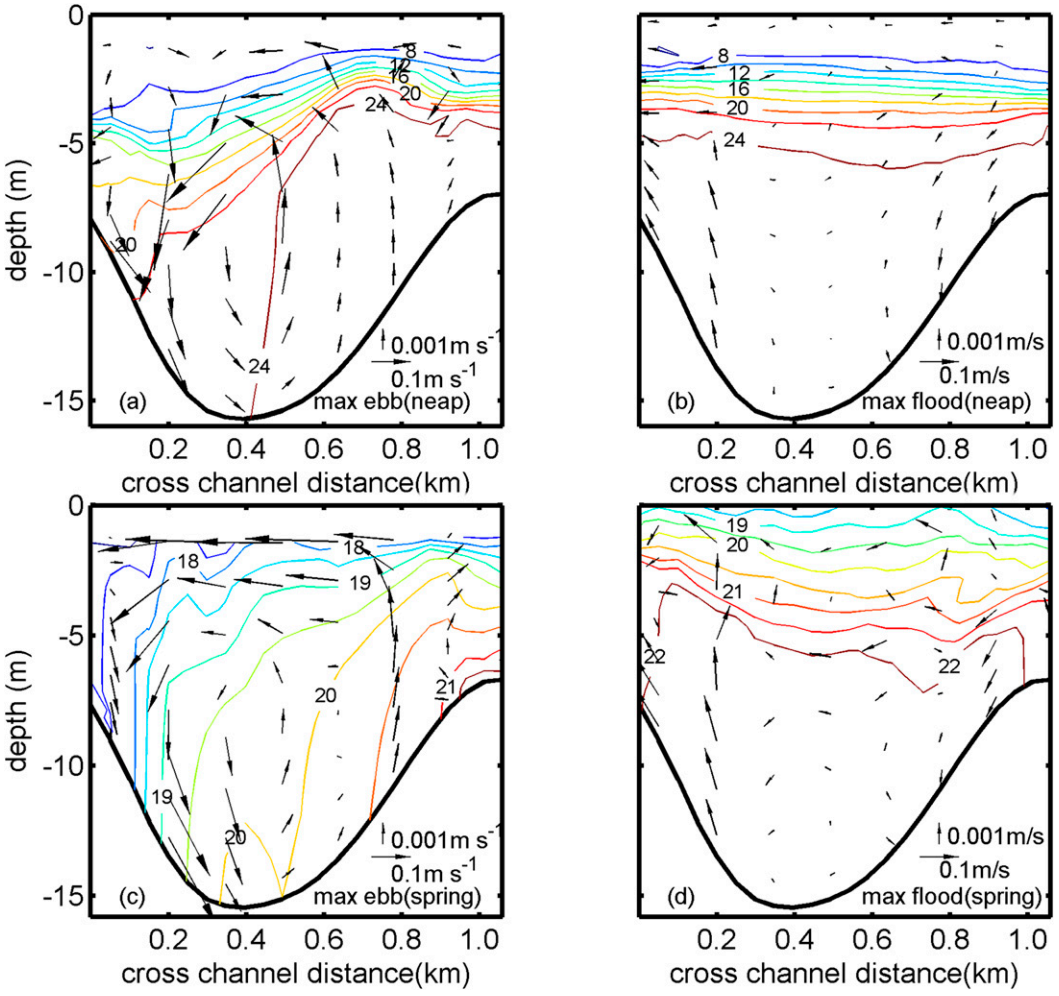


FIG. 13. Instantaneous tidal velocity and salinity structures at section D at (a) maximum ebb during neap tide, (b) maximum flood during neap tide, (c) maximum ebb during spring tide, and (d) maximum flood during spring tide.

density; $h$ is the water depth; $R_s$ is the local radius of curvature of the streamline (positive for clockwise curvature); $u_s$ is the streamwise velocity; $u_n$ is transverse velocity; and $u_s \gg u_n$. Estimates of the terms in Eq. (13) indicate that the centrifugal term [the first term on the rhs of Eq. (13)] and Coriolis term [the second term on the rhs of Eq. (13)] dominate and reinforce each other during maximum ebb, resulting in a strongly secondary flow that is inward to the bend at the bottom and outward at surface. This secondary flow raises isohalines on the right side and pushes down isohalines on the left side (Fig. 13). At maximum flood, vertical velocity shear is weak and the centrifugal term is the opposite sign of the Coriolis term, so there is no transient lateral circulation formed. The isohalines are almost horizontal (Fig. 13). As mentioned in section 3b, when the isohalines with the same salinities are lower at ebb tide than flood tide, positive tidal oscillatory salt transport is induced; when the isohalines with the same salinities are higher at ebb tide than flood tide, negative tidal oscillatory salt transport is induced. Therefore, positive tidal oscillatory salt transport appears on the left side and negative tidal oscillatory salt transport appears on the right side (Fig. 12). During neap tide, the vertical velocity shear is stronger than spring tide, so the tidal oscillatory salt transport is stronger during neap tide than spring tide.

## 4. Discussion

### *a. Distortion of Eulerian framework*

During neap tide, the large longitudinal variation of exchange flow indicates large cross-interface subtidal transport (Fig. 2a), and the vertical position of interface is regarded as constant in one tidal cycle under the Eulerian framework. However, as mentioned in section 3b, the vertical position of interface is not constant but time

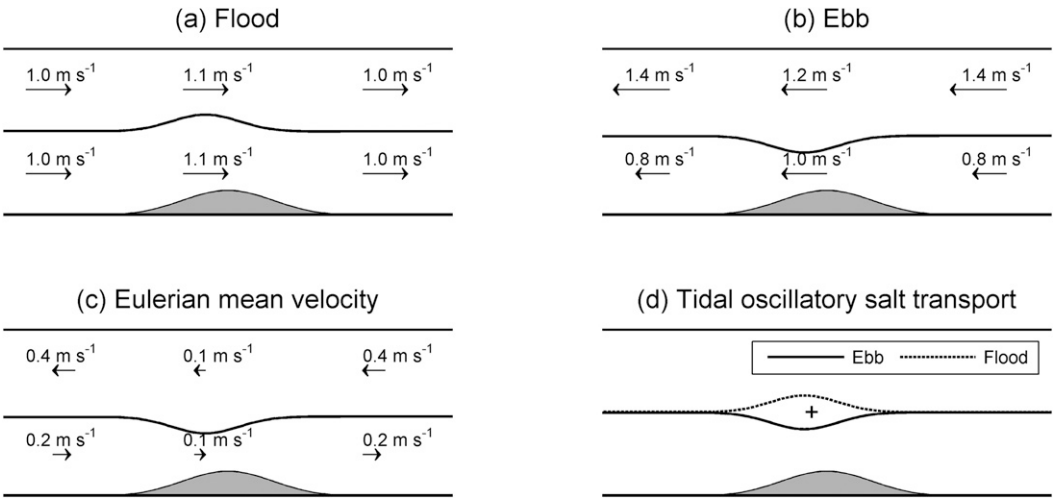


FIG. 14. Schematic of the distortion of subtidal transport in the Eulerian framework and the mechanism of tidal oscillatory salt transport due to hydraulic adjustment, following Geyer and Nepf (1996). The rigid-lid assumption is used in this schematic and the tidal cross-interface transport is assumed as 0. (a) During flood tide, the transports and velocities are uniform in both layers and when the tide flows above a sill, the interface rises due to hydraulic adjustment, and the velocities of both layers increase because of the decreasing of thicknesses of both layers. (b) During ebb tide, the magnitude of velocity in the upper layer is larger than the lower layer because of the river discharge. When the tide flows above the sill, the interface depresses due to hydraulic adjustment, the velocity in the lower layer increases as the thickness of lower layer decreases, and the velocity in the upper layer decreases as the thickness of upper layer increases. (c) According to the Eulerian decomposition method, the Eulerian mean velocity is obtained. The longitudinal variation of the Eulerian mean transport in the lower layer indicates the subtidal cross-interface transport, which conflicts with the assumption. (d) The mechanism of tidal oscillatory salt transport due to hydraulic adjustment. The halocline (interface) is higher during flood tide than ebb tide, so positive tidal oscillatory salt transport is induced.

dependent due to hydraulic adjustment. As shown in Fig. 14, even based on the assumption that no tidal volume transport crosses the interface, the large longitudinal variation of exchange flow obtained the under Eulerian framework still occurs. This mechanism can be explained as follows.

The vertical position of the interface varies through the tidal cycle due to hydraulic adjustment when it flows above a sill. Based on the assumption that no tidal volume transport crosses the interface, the physically reasonable method of calculating the subtidal inflow volume of the lower layer is to first obtain the tidally varying volume transport under the interface and then to find the tidal average. However, when exchange flow and cross-sectionally integrated estuarine salt transport $F_E$ are obtained in the Eulerian framework, the tidal variation of the vertical position of interface causes tidal variation in the transport of each layer, and thus large longitudinal variation of exchange flow obtained under Eulerian framework occurs. This variability in the Eulerian exchange flow is exactly matched by the strong tidal oscillatory salt transport, which is induced because of the tidal variation of the vertical position of the interface. Therefore, the large longitudinal variations in $F_E$ and $F_T$ compensate for each other.

The above analysis demonstrates that during neap tide, the strong transport across the interface in the subtidal time scale showed in an Eulerian framework is mainly due to tidal variation of the position of halocline and not due to any actual flux between the upper and lower layers. As a mathematically compensating term with the cross-sectionally integrated estuarine salt transport $F_E$, the tidal oscillatory salt transport is mainly due to tidal advection and does not represent an independent mechanism from the estuarine exchange flow during neap tide in the Hudson estuary. Because hydraulic adjustment is associated with the topography, strong tidal oscillatory salt transport is mainly a local phenomenon (Fig. 10).

During spring tide, oscillatory shear dispersion is the main mechanism of tidal oscillatory salt transport because of the weak stratification, which is a distinct mechanism and it fundamentally depends on cross-isohaline salt transport.

### b. *Isohaline framework*

Because of the existence of tidal oscillatory salt transport, the salt transport driven by river flow and exchange flow obtained in an Eulerian framework does not satisfy the Knudsen relationship (Knudsen 1900) for

the steady-state salt balance. This analysis indicates that the Knudsen relationship may be satisfied with a Lagrangian representation of the salt transport, in which the tidal oscillatory salt transport is represented as part of the tidally averaged, Lagrangian residual salt transport.

MacCready (2011) proposed a quasi-Lagrangian method for calculating subtidal estuarine exchange flow using an isohaline framework, which is defined as the total exchange flow (TEF) because it contains the contribution of tidal oscillatory salt transport. The TEF decomposition method is shown as follows.

The tidally averaged volume transport through a cross section with salinity greater than $s$ is defined as

$$Q(s) \equiv \left\langle \int_{As} u\, dA \right\rangle, \tag{14}$$

where $As$ is the tidally varying region of the cross section with salinity greater than $s$. Then the volume flux in a specific salinity class can be obtained by differentiating $Q$ with respect to salinity:

$$\frac{\partial Q}{\partial s} = \lim_{\delta s \to 0} \frac{Q(s + \delta s/2) - Q(s - \delta s/2)}{\delta s}. \tag{15}$$

In this paper, we use finite salinity bins with $\delta s$ of 1 psu to calculate $\partial Q/\partial s$. The inflow and outflow of TEF can be defined as

$$Q_{\text{in}}^{\text{TEF}} = \int -\frac{\partial Q}{\partial s}\bigg|_{\text{in}} ds, \quad \text{and} \tag{16a}$$

$$Q_{\text{out}}^{\text{TEF}} = \int -\frac{\partial Q}{\partial s}\bigg|_{\text{out}} ds, \tag{16b}$$

where, "in" means, we only count $-\partial Q/\partial s$ in the integral when it brings water into the estuary. We call the isohaline between the inflow and outflow salinity classes the critical isohaline. The salt flux due to TEF is

$$F_{\text{in}}^{\text{TEF}} = \int s\left(-\frac{\partial Q}{\partial s}\right)\bigg|_{\text{in}} ds, \tag{17a}$$

$$F_{\text{out}}^{\text{TEF}} = \int s\left(-\frac{\partial Q}{\partial s}\right)\bigg|_{\text{out}} ds. \tag{17b}$$

In magnitude, the subtidal salt transport across the cross section driven by TEF is equivalent to the sum of the Eulerian mean and tidal oscillatory salt transport obtained under the Eulerian framework. Based on an isohaline coordinate, it accounts for the time-varying isohaline displacements and thereby combines the Eulerian-averaged and tidal oscillatory contributions to the subtidal salt transport. Using the same calculating methods as MacCready (2011) and Chen et al. (2012), we obtained TEF during neap and spring tides in the Hudson estuary (Fig. 15a). During neap tide, TEF (Fig. 15a) is much smoother than exchange flow obtained in the Eulerian framework (Fig. 15a), which indicates that the subtidal cross-critical isohaline transport is very small. The vertical position of the critical isohaline is almost the same as the halocline, and the halocline indicates the isohaline where $\partial s/\partial z$ reaches its maximum. For example, the salinity of critical isohaline is 16 psu in the region from 13 to 17 km, which is just the salinity of halocline in this region. During spring tides, the magnitude of TEF is close to the Eulerian exchange flow, as the tidal oscillatory salt transport is weak.

Considering TEF per se does not distinguish between shear dispersive and Lagrangian advective transport, the diahaline salt transport would have to be quantified in order to separate pure Lagrangian advection from shear dispersion. The diahaline salt transport across the halocline can be calculated by

$$w_{se} B s_i = -\frac{\partial \int_{A(s_i)} s\, dA}{\partial t} - \frac{\partial \int_{A(s_i)} us\, dA}{\partial x}, \tag{18}$$

where $w_{se}$ indicates the tidally varied effective entrainment velocity across the halocline corresponding to the diahaline salt transport; $B$ is the lateral length of the halocline; $s_i$ indicates the salinity of halocline; and $A(s_i)$ is the tidally varied portion of one cross section with salinity greater than $s_i$. According to the model output, in the lower Hudson estuary, the tidally averaged magnitude of $w_{se}$ is about $1 \times 10^{-5}\,\text{m s}^{-1}$ during neap tide and $1 \times 10^{-4}\,\text{m s}^{-1}$ during spring tide. If we define the tidally averaged diahaline exchange across the halocline in a longitudinal length $L$ as

$$Q_v = \langle w_{se} \rangle BL, \tag{19}$$

where $\langle\ \rangle$ denotes the tidal average, then for the characteristic length scale of longitudinal variation of tidal oscillatory salt transport, which is about 2 km, as shown in Fig. 2b, $Q_v$ is estimated at about $20\,\text{m}^3\,\text{s}^{-1}$ during neap tide. This is much smaller than $Q_{\text{in}}$, so the along-isohaline advection is much larger than the cross-halocline transport. The tidal oscillatory salt transport is mainly due to Lagrangian advection, not dispersion. During spring tide, $Q_v$ is estimated at about $200\,\text{m}^3\,\text{s}^{-1}$, which is in the same order with $Q_{\text{in}}$. Therefore, cross-halocline transport cannot be neglected as a contributor to the tidal oscillatory salt transport during spring tides.

On the other hand, if we use $h/\langle|w_{se}|\rangle$ to estimate the vertical mixing time scale, where $|\ |$ denotes absolute value, we can get the ratio of the mixing time scale to tidal time scale as about 1 during spring tide and much

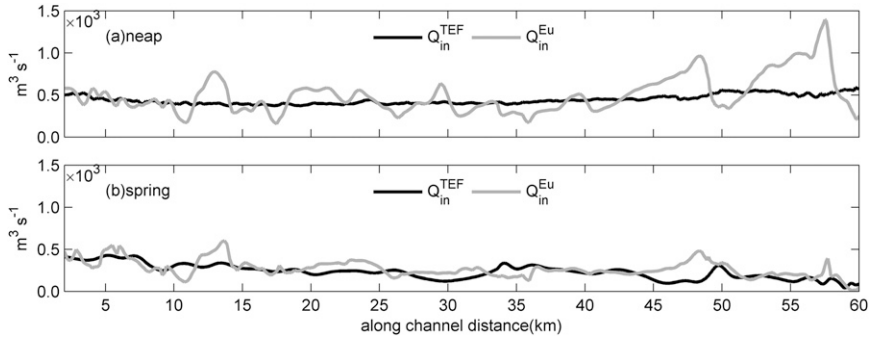


FIG. 15. Inflow volume of exchange flow obtained in the Eulerian framework (EU) and the isohaline framework (TEF) during (a) neap and (b) spring tides. A 33-h low-pass filter is used to obtain the tidally averaged values.

smaller than 1 during neap tide. This is consistent with the result obtained by the vertical diffusivity that the mixing time scale is in the optimal range for contributing to oscillatory shear dispersion during spring tides.

Although TEF is not exactly Lagrangian, it does provide insight into the Lagrangian transport, and it is useful for quantifying the salt transport across the halocline. The TEF may hold promise for better understanding the exchange process in estuaries, for instance by comparing the TEF with a Lagrangian residual framework (Zimmerman 1979; Feng et al. 2008; Jiang and Feng 2011, 2014; Lemagie and Lerczak 2014).

## 5. Conclusions

In this paper, we examined the mechanisms of tidal oscillatory salt transport in the Hudson estuary by utilizing a numerical model. The results show that there are multiple mechanisms influencing the tidal oscillatory salt transport during the neap–spring cycle, with the main mechanism changing from hydraulic adjustment during neap tide to tidal shear dispersion during spring tide. During neap tide, the Eulerian decomposition results in a large and spatially variable tidal oscillatory salt transport that is largely the result of purely advective, that is, nondispersive, salt transport caused by vertical motion of the halocline. This vertical motion is due to a combination of internal hydraulic forcing over topography and curvature-induced secondary flow. During spring tide, tidal oscillatory salt transport has less spatial variability, and it has a more significant net contribution because of the oscillatory shear dispersion.

The tidal oscillatory salt transport can be regarded as part of subtidal salt transport in a Lagrangian framework. The exchange flow obtained from the Eulerian framework shows extreme spatial variability that does not represent a unique process but rather results from leaving out a large fraction of the total or Lagrangian salt transport in the Eulerian averaging process. The isohaline framework is an alternative way to provide a consistent and physically realistic representation of the subtidal salt transport. When the diahaline salt transport is large enough to make the mixing time scale comparable to the tidal time scale, tidal dispersion contributes much to the tidal oscillatory salt transport. When the diahaline salt transport is small, Lagrangian advection is the main mechanism.

*Acknowledgments.* Tao Wang was supported by the Open Research Fund of State Key Laboratory of Estuarine and Coastal Research (Grant SKLEC-KF201509) and Chinese Scholarship Council. Geyer was supported by by NSF Grant OCE 0926427. Wensheng Jiang was supported by NSFC-Shandong Joint Fund for Marine Science Research Centers (Grant U1406401). We would like to acknowledge Yizhen Li for his advice on this paper. We acknowledge the comments of three anonymous reviewers.

## REFERENCES

Bowden, K. F., 1965: Horizontal mixing in the sea due to a shearing current. *J. Fluid Mech.*, **21**, 83–95, doi:10.1017/S0022112065000058.

Bowen, M. M., and W. R. Geyer, 2003: Salt transport and the time-dependent salt balance of a partially stratified estuary. *J. Geophys. Res.*, **108**, 3158, doi:10.1029/2001JC001231.

Chen, S.-N., W. R. Geyer, D. K. Ralston, and J. A. Lerczak, 2012: Estuarine exchange flow quantified with isohaline coordinates: Contrasting long and short estuaries. *J. Phys. Oceanogr.*, **42**, 748–763, doi:10.1175/JPO-D-11-086.1.

Díez-Minguito, M., E. Contreras, M. J. Polo, and M. A. Losada, 2013: Spatio-temporal distribution, along-channel transport, and post-riverflood recovery of salinity in the Guadalquivir estuary (SW Spain). *J. Geophys. Res. Oceans*, **118**, 2267–2278, doi:10.1002/jgrc.20172.

Dronkers, J., and J. Van De Kreeke, 1986: Experimental determination of salt intrusion mechanisms in the Volkerak estuary. *Neth. J. Sea Res.*, **20**, 1–19, doi:10.1016/0077-7579(86)90056-6.

Dyer, K. R., 1997: Salt balance. *Estuaries: A Physical Introduction*, 2nd ed. John Wiley and Sons, 69–85.

Engel, P. A., 2009: Spatial and temporal variability of tide-induced salt flux in a partially mixed estuary. M. S. thesis, Dept. of Earth, Atmospheric, and Planetary Sciences, Massachusetts Institute of Technology/Woods Hole Oceanographic Institution Joint Program in Oceanography/Applied Ocean Science and Engineering, 45 pp.

Feng, S., L. Ju, and W. Jiang, 2008: A Lagrangian mean theory on coastal sea circulation with inter-tidal transports. I. Fundamentals. *Acta Oceanol. Sin.*, **27**, 1–16.

Fischer, H. B., 1972: Mass transport mechanisms in partially stratified estuaries. *J. Fluid Mech.*, **53**, 671–687, doi:10.1017/S0022112072000412.

——, 1976: Mixing and dispersion in estuaries. *Annu. Rev. Fluid Mech.*, **8**, 107–133, doi:10.1146/annurev.fl.08.010176.000543.

——, E. J. List, R. C. Y. Koh, J. Imberger, and N. A. Brooks, 1979: *Mixing in Inland and Coastal Waters*. Academic Press, 483 pp.

Geyer, W. R., 1993: Three-dimensional tidal flow around headlands. *J. Geophys. Res.*, **98**, 955–966, doi:10.1029/92JC02270.

——, and H. Nepf, 1996: Tidal pumping of salt in a moderately stratified estuary. *Buoyancy Effects on Coastal and Estuarine Dynamics*, Coastal and Estuarine Studies Series, Vol. 53, Amer. Geophys. Union, 213–226, doi:10.1029/CE053p0213.

——, and D. K. Ralston, 2011: The dynamics of strongly stratified estuaries. *Water and Fine Sediment Circulation*, R. J. Uncles and S. G. Monismith, Eds., Vol. 2, *Treatise on Estuarine and Coastal Science*, Academic Press, 37–51, doi:10.1016/B978-0-12-374711-2.00206-0.

——, R. Chant, and R. Houghton, 2008: Tidal and spring-neap variations in horizontal dispersion in a partially mixed estuary. *J. Geophys. Res.*, **113**, C07023, doi:10.1029/2007JC004644.

Giddings, S. N., S. G. Monismith, D. A. Fong, and M. T. Stacey, 2014: Using depth-normalized coordinates to examine mass transport residual circulation in estuaries with large tidal amplitude relative to the mean depth. *J. Phys. Oceanogr.*, **44**, 128–148, doi:10.1175/JPO-D-12-0201.1.

Hansen, D. V., and M. Rattray, 1965: Gravitational circulation in straits and estuaries. *J. Mar. Res.*, **23**, 104–122.

Jay, D. A., 1991: Estuarine salt conservation: A Lagrangian approach. *Estuarine Coastal Shelf Sci.*, **32**, 547–565, doi:10.1016/0272-7714(91)90074-L.

Jiang, W., and S. Feng, 2011: Analytical solution for the tidally induced Lagrangian residual current in a narrow bay. *Ocean Dyn.*, **61**, 543–558, doi:10.1007/s10236-011-0381-z.

——, and ——, 2014: 3D analytical solution to the tidally induced Lagrangian residual current equations in a narrow bay. *Ocean Dyn.*, **64**, 1073–1091, doi:10.1007/s10236-014-0738-1.

Knudsen, M., 1900: Ein hydrographischer Lehrsatz. *Ann. Hydrogr. Marit. Meteor.*, **28**, 316–320.

Larsen, L. H., 1977: Dispersion of a passive contaminant in oscillatory fluid flows. *J. Phys. Oceanogr.*, **7**, 928–930, doi:10.1175/1520-0485(1977)007<0928:DOAPCI>2.0.CO;2.

Lemagie, E. P., and J. A. Lerczak, 2014: A comparison of bulk estuarine turnover timescales to particle tracking timescales using a model of the Yaquina Bay estuary. *Estuaries Coasts*, **38**, 1797–1814, doi:10.1007/s12237-014-9915-1.

Lerczak, J. A., W. R. Geyer, and R. J. Chant, 2006: Mechanisms driving the time-dependent salt flux in a partially stratified estuary. *J. Phys. Oceanogr.*, **36**, 2296–2311, doi:10.1175/JPO2959.1.

MacCready, P., 1999: Estuarine adjustment to changes in river flow and tidal mixing. *J. Phys. Oceanogr.*, **29**, 708–726, doi:10.1175/1520-0485(1999)029<0708:EATCIR>2.0.CO;2.

——, 2004: Toward a unified theory of tidally-averaged estuarine salinity structure. *Estuaries*, **27**, 561–570, doi:10.1007/BF02907644.

——, 2007: Estuarine adjustment. *J. Phys. Oceanogr.*, **37**, 2133–2144, doi:10.1175/JPO3082.1.

——, 2011: Calculating estuarine exchange flow using isohaline coordinates. *J. Phys. Oceanogr.*, **41**, 1116–1124, doi:10.1175/2011JPO4517.1.

——, and W. R. Geyer, 2010: Advances in estuarine physics. *Annu. Rev. Mar. Sci.*, **2**, 35–58, doi:10.1146/annurev-marine-120308-081015.

McCarthy, R. K., 1993: Residual currents in tidally dominated, well-mixed estuaries. *Tellus*, **45A**, 325–340, doi:10.1034/j.1600-0870.1993.00007.x.

Okubo, A., 1973: Effect of shoreline irregularities on streamwise dispersion in estuaries and other embayments. *Neth. J. Sea Res.*, **6**, 213–224, doi:10.1016/0077-7579(73)90014-8.

Ou, H. W., C. M. Dong, and D. Chen, 2000: On the tide-induced property flux: Can it be locally countergradient? *J. Phys. Oceanogr.*, **30**, 1472–1477, doi:10.1175/1520-0485(2000)030<1472:OTTIPF>2.0.CO;2.

Pritchard, D. W., 1954: A study of the salt balance in a coastal plain estuary. *J. Mar. Res.*, **13**, 133–144.

Robinson, I. S., 1983: Tidally induced residual flows. *Physical Oceanography of Coastal and Shelf Seas*, B. Johns, Eds., Elsevier Oceanography Series, Vol. 35, Elsevier, 321–356.

Schijf, J. B., and J. C. Schonfeld, 1953: Theoretical consideration on the motion of salt and fresh water. *Proc. Minnesota Int. Hydraulic Conf.*, Minneapolis, Minnesota, ASCE, 321–333.

Stommel, H. M., and H. G. Former, 1952: On the nature of estuarine circulation. Part I. Woods Hole Oceanographic Institution Ref. 52–88, 172 pp. [Available online at https://darchive.mblwhoilibrary.org/handle/1912/2032.]

Taylor, G., 1954: The dispersion of matter in turbulent flow through a pipe. *Proc. Roy. Soc. London*, **A223**, 446–468, doi:10.1098/rspa.1954.0130.

Thorne, C. R., and R. D. Hey, 1979: Direct measurements of secondary currents at a river inflexion point. *Nature*, **280**, 226–228, doi:10.1038/280226a0.

Uncles, R. J., R. C. A. Elliott, and S. A. Weston, 1985: Dispersion of salt and suspended sediment in a partly mixed estuary. *Estuaries*, **8**, 256–269, doi:10.2307/1351486.

Warner, J. C., W. R. Geyer, and J. A. Lerczak, 2005: Numerical modeling of an estuary: A comprehensive skill assessment. *J. Geophys. Res.*, **110**, C05001, doi:10.1029/2004JC002691.

Zimmerman, J. T. F., 1979: On the Euler-Lagrange transformation and the Stokes' drift in the presence of oscillatory and residual currents. *Deep-Sea Res.*, **26A**, 505–520, doi:10.1016/0198-0149(79)90093-1.

——, 1986: The tidal whirlpool: A review of horizontal dispersion by tidal and residual currents. *Neth. J. Sea Res.*, **20**, 133–154, doi:10.1016/0077-7579(86)90037-2.